A&A, 695, A44 (2025)
https://doi.org/10.1051/0004-6361/202452243

Astronomy & Astrophysics

NICER observations of type-I X-ray bursts from the ultra-compact X-ray binary M15 X-2

María Alejandra Díaz Teodori[1,2,★], Jari J. E. Kajava[3], Celia Sánchez-Fernández[4], Andrea Sanna[5], Mason Ng[6,7,8], and Juri Poutanen[1]

[1] Department of Physics and Astronomy, FI-20014 University of Turku, Finland
[2] Nordic Optical Telescope, Rambla José Ana Fernández, Pérez 7, E-38711 Breña Baja, Spain
[3] Serco for the European Space Agency (ESA), European Space Astronomy Centre, Camino Bajo del Castillo s/n, E-28692 Villanueva de la Cañada, Madrid, Spain
[4] ATG Europe for the European Space Agency (ESA), European Space Astronomy Centre, Camino Bajo del Castillo s/n, E-28692 Villanueva de la Cañada, Madrid, Spain
[5] Dipartimento di Fisica, Universitá degli Studi di Cagliari, SP Monserrato-Sestu km 0.7, I-09042 Monserrato, Italy
[6] MIT Kavli Institute for Astrophysics and Space Research, Massachusetts Institute of Technology, 77 Massachusetts Avenue, Cambridge, MA 02139, USA
[7] Department of Physics, McGill University, 3600 rue University, Montréal, QC H3A 2T8, Canada
[8] Trottier Space Institute, McGill University, 3550 rue University, Montréal, QC H3A 2A7, Canada

Received 13 September 2024 / Accepted 1 January 2025

ABSTRACT

Type-I X-ray bursts are thermonuclear explosions caused by the unstable burning of accreted material on the surface of neutron stars. We report the detection of seven type-I X-ray bursts from the ultracompact X-ray binary M15 X-2 observed by the Neutron Star Interior Composition Explorer (NICER) during its 2022 outburst. We found all the bursts occurred in the soft state and exhibited similar light curve profiles, with no cases of photospheric radius expansion. Time-resolved spectroscopy showed clear deviations from the blackbody model during the first ten seconds of all the bursts. The fits were improved by using the enhanced persistent emission 'f_a' method, which we interpret as evidence of burst-disk interaction. We compared the performance of these models against a neutron star atmosphere model and found it made no significant improvements. After analyzing the burst rise times and fuel composition, we propose that these bursts were powered by the burning of pure helium, confirming the ultracompact nature of the source.

Key words. accretion, accretion disks – stars: neutron – X-rays: binaries – X-rays: bursts – X-rays: individuals: M15 X-2

1. Introduction

Since their discovery in 1976 (Grindlay et al. 1976), type-I X-ray bursts (hereafter, X-ray bursts) have been a key tool in the study of neutron stars (NSs), offering insights into both their accretion processes and intrinsic characteristics. These bursts are thermonuclear explosions that take place in low-mass X-ray binary (LMXB) systems with a NS primary. They are caused by the accretion of matter from the low-mass companion onto the NS, which creates a fuel layer on the NS surface that grows and compresses until the conditions for thermonuclear ignition are reached (see reviews in Lewin et al. 1993; Strohmayer & Bildsten 2006; Galloway & Keek 2021).

X-ray bursts are manifested as a sudden increase in X-ray emission followed by an exponential decay, usually lasting ∼10–100 s (Lewin et al. 1993). In rare instances, there are bursts of longer duration: intermediate-duration bursts last from minutes to an hour, and superbursts can last many hours (e.g., Strohmayer & Brown 2002; Cumming et al. 2006). The burst duration is related to the depth and composition of the fuel layer. Moreover, both the H/He ratio (Fujimoto et al. 1981; Galloway & Keek 2021) and the metallicity (Heger et al. 2007) impact the burst timescale, since both of these properties affect the nuclear-burning pathways.

Through time-resolved spectroscopy of X-ray bursts, insights can be gained into the properties of the NS and its accretion environment. The spectrum of the system during an X-ray burst is usually modeled by the sum of the persistent emission spectrum, which is assumed to not vary during the burst (e.g., Lewin et al. 1993), and a blackbody component, with evolving parameters to describe the burst itself.

During the initial fuel ignition, the measured blackbody temperature increases to a maximum of 2–3 keV and then gradually decreases as the flux drops and the photosphere cools down. Nonetheless, numerous bursts show deviations from the traditional model (van Paradijs et al. 1990), either due to changes in the persistent emission (Worpel et al. 2013, 2015) or the intrinsic burst spectrum (e.g., Kajava et al. 2017; Sánchez-Fernández et al. 2020). The radiation produced during X-ray bursts may interact with the accretion disk. In this context, several phenomena that could affect the persistent emission have been studied, namely: radiatively driven outflows (e.g., Degenaar et al. 2013), increased inflow rate due to the Poynting-Robertson drag (Worpel et al. 2013), and changes in the disk structure due to burst heating (e.g., Ballantyne & Everett 2005; in't Zand et al. 2011). To account for enhanced persistent emission, Worpel et al. (2013) and in't Zand et al. (2013) proposed the "f_a" method, which involves adding a multiplicative factor f_a to the persistent emission model when fitting the spectra.

★ Corresponding author; madiazteo@gmail.com

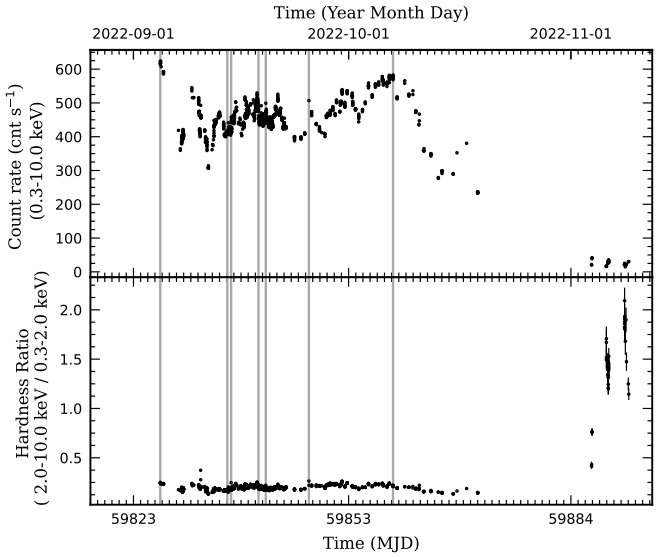

Fig. 1. Properties of M15 X-2 outburst detected by NICER in the 0.3–10 keV energy band. *Top panel*: the light curve. *Bottom panel*: Hardness ratio of the count rates between the 2–10 and 0.3–2.0 keV energy bands. The X-ray bursts have been removed from the light curve, but the detection time of each burst is marked with a grey vertical line. For the fifth burst, only the tail was observed, so the onset is an approximation based on Fig. 3.

Worpel et al. (2013, 2015) applied this method to a large sample of bursts and found enhanced persistent emission to be common. This method, however, assumes that the shape of the persistent emission does not change during the burst. Regarding the intrinsic burst spectrum, the emission from hot NS atmospheres is not expected to be an ideal blackbody: the combined effect of Compton scattering and free-free (and bound-free) emission and absorption in the NS atmosphere modifies the spectrum into a diluted blackbody (e.g., London et al. 1986; Suleimanov et al. 2012).

M15 X-2 is one of the three known X-ray sources in the globular cluster (GC) M15, along with AC 211 (White & Angelini 2001) and M15 X-3 (Heinke et al. 2009). M15 X-2 and AC 211 are persistent sources (Heinke et al. 2024), whereas M15 X-3 is a faint transient. M15 X-2 is also an ultracompact X-ray binary (UCXB) system. UCXBs are defined by their short orbital periods ($\lesssim$60–80 min) that cannot fit hydrogen-rich companions (Nelson et al. 1986) and instead have donors ranging from white dwarfs (WDs) to helium stars to evolved main-sequence stars (e.g., Yungelson et al. 2002; Nelemans et al. 2006).

The discovery of M15 X-2 is closely tied to AC 211 and, in fact, it helped resolve the decade-long mystery surrounding AC 211. The LMXB AC 211 is known for its edge-on inclination, obscuring the central X-ray source behind the accretion disk. This became a source of confusion in 1988, when the *Ginga* satellite detected a very potent X-ray burst (van Paradijs et al. 1990) from AC 211, an event that should have been concealed by the disk. Similarly, the Rossi X-ray Timing Explorer (RXTE) detected another powerful burst in 2000 (Smale 2001). Eventually, White & Angelini (2001), through *Chandra* observations, discovered that the bursts were actually coming from M15 X-2, which was 2.″7 away from AC 211 and had been previously unresolved.

Four years later, Dieball et al. (2005) determined the period of the far-ultraviolet (FUV) counterpart of M15 X-2 to be ~23 min, confirming it as a UCXB. Additionally, they found FUV evidence of C and/or He lines. Later on, Koliopanos et al. (2021) studied the X-ray spectrum of M15 X-2 and found no Fe Kα line emission, which they concluded was evidence of a C/O or O/Ne/Mg WD donor. Thus, the hydrogen-poor nature of the companion was confirmed, but its exact classification remained unclear.

Since its identification in 2001, bursts from M15 X-2 have been observed again in 2003 by *Beppo*SAX/WFC (Kuulkers et al. 2003), as well as in 2011 by the Monitor of All-sky X-ray Image (MAXI; Miller-Jones et al. 2011; Sivakoff et al. 2011) and in 2013 again by MAXI (Tomida et al. 2013; Pooley & Homan 2013). Additionally, Charles et al. (2002) identified 15 burst candidates in archival All Sky Monitor/RXTE data.

On 2022 August 26, after almost a decade in a low state, a new outburst from the M15 field was detected by MAXI/Gas Slit Camera (Ng et al. 2022). On 2022 September 4, the Neutron Star Interior Composition Explorer (NICER) performed a 1.6 ks observation of M15 and observed one X-ray burst. On 2022 September 27, *Chandra*/ACIS-S conducted follow-up observations and concluded M15 X-2 was the source of the outburst and subsequent X-ray burst (Homan et al. 2022). NICER continued carrying out follow-up observations until 2022 November 9.

In this work, we report the analysis of seven X-ray bursts from M15 X-2 observed by NICER during its 2022 outburst. In Sect. 2, we describe the observational data and reduction procedure. In Sect. 3, we present the spectral and timing analysis results. In Sect. 4, we discuss the results obtained and in Sect. 5, we summarize the main conclusions of the study.

Table 1. Basic information on the seven bursts.

Burst	ID	Burst Onset (MJD)
1	5034140101	59826.73942
2	5034140110	59836.09463
3	5034140110	59836.61754
4	5034140114	59840.43209
5	5034140115 [(a)]	59841.45299
6	5034140121	59847.46255
7	5034140131	59859.19994

Notes. Time is in TT system. [(a)]The onset is approximate, based on Fig. 3, because only the tail of this burst was observed.

2. Observations

We analyzed the 51 M15 X-2 NICER observations (ObsIDs 5034140101-5034140152) that monitored the outburst between August and November 2022 (see Fig. 1). The total coverage was 146.8 ks. We found seven bursts, with the corresponding ObsIDs and burst onset times given in Table 1.

We processed the data using HEASOFT v 6.31.1 and the NICER Data Analysis Software NICERDAS. This was done through the use of HEASoftPy, a PYTHON 3 package, which gives access to the HEASOFT tools. The processing consists of several steps, with the first being the use of standard NICER-recommended calibration and filtering tool NICERL2 to produce the clean event files. Standard screening criteria were applied, which include a pointing offset of <54″, Earth limb elevation angle of >15°, elevation angle with respect to the bright Earth limb of >30°, being outside of the South Atlantic Anomaly, and an overshoot rate of <1 cnt s^{-1} per detector. Since the HEASOFT v6.31. release, NICERL2 requires updated geomagnetic

quantities; in this case, we have used data from NOAA's Space Weather Prediction Center.

From the event files, the light curves were produced using the HEASOFT task `extractor` with 1 s binning. It was checked beforehand that all 52 NICER detectors were enabled throughout the observations. Bursts were detected by performing sigma-clipping with a 5σ limit. In the intervals where a burst was detected, the onset time was obtained through the following procedure: 1) finding the peak of the burst; 2) calculating the average persistent emission by averaging between −40 s and −20 s before burst peak time (this timescale ensured we could study bursts, e.g., Burst 3, which occurred <50 s after the observation onset); 3) subtracting the persistent emission to the light-curve; 4) dividing the light curve by the peak value of the burst, such that it was now normalized; and 5) starting from the peak, searching backward until we found the first point where the amplitude went below 0.1, that being the onset time. If there is not enough data to go back 40 s, we averaged the first 5 s of the observation.

To determine the rise and decay timescales of the burst, the individual light curves were fitted by applying the phenomenological model proposed by Pike et al. (2021). This work uses a piecewise approach in which a fast-rise exponential-decay (FRED) curve models the rise, peak, and beginning of the decay, and the later decay is modeled as a power law. This allows us to model the X-ray burst signature quick rise and slower decay, while also taking into consideration the later decay of X-ray bursts more closely resembles a power law, as shown, for example, by in't Zand et al. (2017). The model is expressed as:

$$f(t) = \begin{cases} A \exp\left[-\dfrac{\tau_{\rm R}}{t} - \dfrac{t}{\tau_{\rm D}}\right] + C, & t \leq t_{\rm tail}, \\ B\left(\dfrac{t}{t_{\rm tail}}\right)^{-\gamma} + C, & t > t_{\rm tail}, \end{cases} \tag{1}$$

where A is the peak intensity, $\tau_{\rm R}$ is the rise timescale, $\tau_{\rm D}$ is the decay timescale, $t_{\rm tail}$ is the transition time from exponential to the power-law tail, γ is the power-law index, and $B \equiv A \exp\left[-\frac{\tau_{\rm R}}{t_{\rm tail}-t_0} - \frac{t_{\rm tail}-t_0}{\tau_{\rm D}}\right]$, which ensures the exponential and the power-law tails have the same count rate at $t = t_{\rm tail}$.

The burst spectra were also produced with `extractor`. For the pre-burst spectra, we extracted 20 s intervals ending at least 20 s before burst onset, the only exception being burst #5, as the onset of the burst happened before our observation started, so the 20 s interval was extracted from the previous observation, approximately 10^4 s before the start of the burst. To perform time-resolved spectroscopy of the burst itself, dynamic intervals containing 1500 counts were generated, and spectra were extracted for each interval. The spectrum files were then binned using the `grppha` tool, with a minimum condition of 20 counts per bin to ensure we are in the domain of chi-square statistics.

To produce the response matrix files (RMF) and ancillary response files (ARF) for the spectral analysis, the NICERDAS tools `nicerrmf` and `nicerarf` were used, respectively. The background was estimated using the `nibackgen3C50` task (Remillard et al. 2022). For this analysis, the NICER calibration files were obtained through the CALDB remote access, and the October 2022 version was used. Once all the necessary files were created, the spectra were analyzed using the PYTHON interface of XSPEC (Arnaud 1996), PyXSPEC.For this purpose, XSPEC v12.13.0 was used. The models used to analyze the spectra will be explained in detail in Sect. 3. Uncertainties were calculated at 1σ confidence level.

3. Analysis and results

3.1. Outburst analysis

The outburst light curve and hardness plot are presented in Fig. 1, encompassing all the observations taken between August and November 2022. The X-ray bursts have been removed from the light curve, but the onset times are marked with vertical grey lines. Six X-ray bursts, plus the tail of the seventh, were identified during this outburst.

In the bottom panel of Fig. 1, we see how the hardness ratio increases significantly near MJD 59889. We extracted spectra for these pointings and noticed that they can be modeled using a DISKBB model of $T_{\rm in} \approx 2$ keV, with partial covering absorber of $N_{\rm H} \sim 10^{22}$ cm^{-2}, a partial covering fraction of about $PCF \approx 0.92$, and 0.3–10 keV flux of $F_{\rm x} \sim 10^{-10}$ erg cm^{-2} s^{-1}. These values are very similar to earlier measurements of the nearby AC 211 (Sidoli et al. 2000; White & Angelini 2001), suggesting that at the end of the NICER observing campaign, AC 211 is already brighter than M15 X-2. If we consider that the outburst lasted until the last observation in the softer state, the duration of the outburst was 54 d.

We studied the persistent emission before each burst by extracting 20 s intervals ending at least 20 s before burst onset. All of the spectra were fit to the model `tbabs*(diskbb+comptt)`. This consists of a multicolor disk blackbody component (`diskbb`, Makishima et al. 1986), combined with a Comptonization component (`comptt`, Titarchuk 1994) and modified by the Tübingen–Boulder interstellar absorption model `tbabs`. We used the element abundances provided by Wilms et al. (2000).

For the `diskbb` component, we allowed both of its parameters, the inner disk radius temperature, $T_{\rm in}$, and the normalization, $K_{\rm diskbb}$, to vary. We fixed the `comptt` seed temperature $T_0 = 1.5$ keV, electron temperature $T_{\rm e} = 3.3$ keV and the optical depth $\tau = 5.0$, following Revnivtsev & Gilfanov (2006). Only the normalization $K_{\rm comptt}$ was allowed to vary. The fitting results for each burst are displayed in Table 2. The average values obtained for the parameters are $N_{\rm H} = (5.6 \pm 0.6) \times 10^{20}$ cm^{-2}, $T_{\rm in} = 0.69 \pm 0.05$ keV, $K_{\rm diskbb} = 140 \pm 30$, and $K_{\rm comptt} = 0.029 \pm 0.007$.

From the average disk normalization, we estimated the apparent inner disk radius $R_{\rm in}$, which is related to each other as $K_{\rm diskbb} = (R_{\rm in}/D_{10})^2 \cos\theta$, where D_{10} is the distance to the source in units of 10 kpc, and θ the disk inclination (Makishima et al. 1986). Using the Gaia EDR3 value of 10.7 kpc for the distance (Baumgardt & Vasiliev 2021) and taking $\theta = 34°$ (Dieball et al. 2005), an average $R_{\rm in} \approx 11$ km is obtained. This is close to a NS radius, which is thought to be between 10 to 15 km.

The persistent spectrum of burst #4 is shown in Fig. 2. The model seems to fit the data with no significant deviations at any point in the energy range. The obtained parameter values are compatible with the soft state (Done et al. 2007).

3.2. Burst light curves

Individual light curves of the seven X-ray bursts were extracted in the 0.3–10 keV energy band with 1 s binning. In Fig. 3, the light curves are displayed overlapping each other, aligned by the burst onset. We see that the bursts display similar morphology, with the count rate peaking at around 2500–3000 cnt s^{-1}.

The results of the fittings of model Eq. (1) to the burst light curves are presented in Table 3. From the derived timescales, we can get the average value of the rise, $\tau_{\rm rise} = 0.10 \pm 0.04$ s, and

Table 2. Best-fit parameters of the model `tbabs*(diskbb+comptt)` for pre-burst spectra of the seven bursts.

Burst	`tbabs` N_H (10^{20} cm^{-2})	`diskbb` T_{in} (keV)	`diskbb` norm	`compTT` norm	Flux (10^{-10} erg cm^{-2} s^{-1})	χ^2/d.o.f.
1	5.0 ± 0.4	0.80 ± 0.03	110 ± 10	0.043 ± 0.003	14.4 ± 0.1	0.86
2	6.4 ± 0.5	0.60 ± 0.02	200 ± 30	0.021 ± 0.002	8.0 ± 0.1	0.98
3	4.9 ± 0.5	0.66 ± 0.02	142 ± 20	0.025 ± 0.002	8.5 ± 0.1	1.07
4	5.5 ± 0.6	0.74 ± 0.02	110 ± 10	0.030 ± 0.002	10.5 ± 0.1	0.87
5	5.7 ± 0.5	0.70 ± 0.02	130 ± 20	0.023 ± 0.002	9.1 ± 0.1	0.98
6	6.1 ± 0.5	0.72 ± 0.02	120 ± 10	0.026 ± 0.002	9.8 ± 0.1	1.06
7	6.0 ± 0.4	0.74 ± 0.02	140 ± 20	0.035 ± 0.003	12.7 ± 0.1	0.95

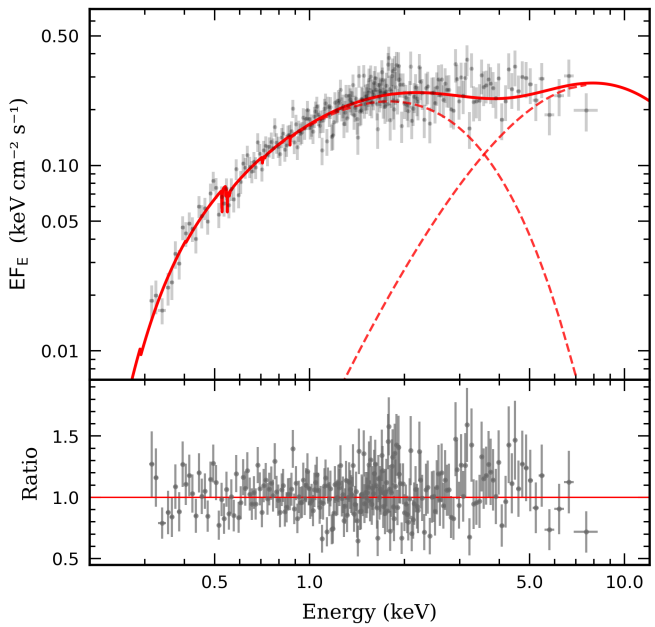

Fig. 2. X-ray spectrum of the pre-burst emission for burst #4. Spectra of other bursts are shown in Fig. A.1. The solid red line represents the total model `tbabs*(diskbb+comptt)`, while the dashed lines represent `diskbb` and `comptt` components separately, and the gray points show the data. The pre-burst emission was chosen as a 20 s interval taking place 20 s before the burst.

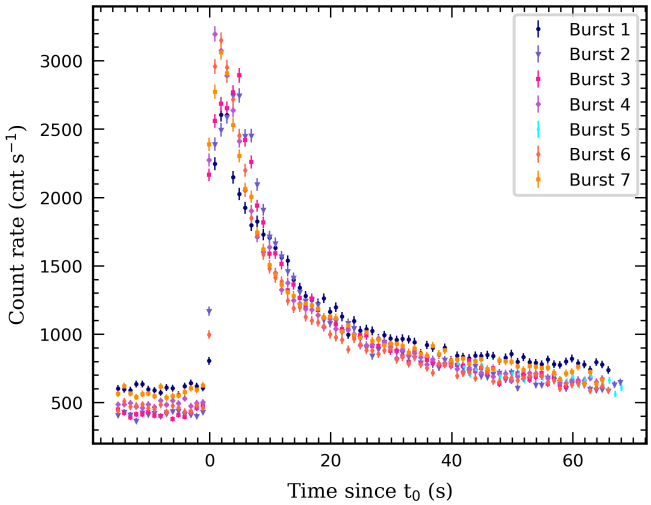

Fig. 3. Overlapped light curves of the seven M15 X-2 bursts in the 0.3–10 keV band with 1 s binning. The light curves are aligned by the burst onset (t_0). Each color and symbol represents a different burst. For burst 5, only the tail was observed, so it was manually positioned to match the morphology of the other bursts.

Table 3. Best-fit rise timescale, decay timescale and power-law value using Eq. (1) to the burst profiles.

Burst	τ_R (s)	τ_D (s)	γ
1	0.0791 ± 0.0004	15 ± 1	1.0770 ± 0.0008
2	0.1289 ± 0.0001	30 ± 5	1.0262 ± 0.0001
3	0.1434 ± 0.0001	28 ± 6	0.9752 ± 0.0001
4	0.04201 ± 0.00004	15.0 ± 0.8	0.9687 ± 0.0001
6	0.08954 ± 0.00006	22 ± 5	0.9754 ± 0.0001

Notes. Burst 5 is omitted because only the tail was observed.

of the decay time, τ_{dec} = 22 ± 7 s. We also see that all bursts have occurred around the same hardness level (see bottom panel of Fig. 1).

It is worth noting that the second and third bursts were observed in a single observation (ObsID 5034140110). In Fig. 4, we show a cropped version of this observation to show the two consecutive bursts. The time between the two bursts is 45 179 ± 1 s (~12.5 h). Additionally, looking at Fig. 1 again, we see that the fourth and fifth bursts are observed quite close to each other, with the time between them being 88 207 ± 1 s (~24.5 h).

Our findings suggest that the recurrence time is unlikely to be half or a quarter of this period, as indicated by the blue and orange arrows in Fig. 4, respectively. These arrows mark telescope pointings during these times, and no bursts were detected. The only scenario that cannot be entirely dismissed is a recurrence time of one-third of the observed interval, shown by the green arrows, due to a lack of pointings during these intervals. However, the fourth and fifth bursts, observed in close succession (Fig. 1), occurred ~24.5 h apart, almost double the proposed recurrence time.

3.3. Time-resolved burst spectroscopy

Time-resolved spectroscopy was performed for each burst using several models. The results for each individual model are discussed below. In all cases the unabsorbed bolometric flux was calculated using the `cflux` model component in XSPEC.

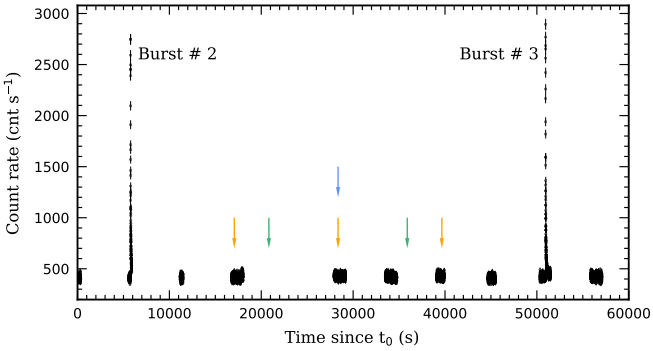

Fig. 4. Cropped light curve of ObsID 5034140110, showing two consecutive X-ray bursts (#2 and #3). Assuming the recurrence time is the interval between the two bursts, the blue arrow indicates where a burst would appear with half the recurrence time, the green arrows where they would appear with a third of the recurrence time, and the orange arrows where they would appear with a fourth of the recurrence time. Time is relative to the onset of the observation t_0 = 59859.1880 MJD (TT).

3.3.1. Blackbody model

We first attempted to model the spectra of all the bursts by adding a blackbody component to the pre-burst spectrum model, holding constant all the parameters except those of the blackbody (i.e., assuming that the pre-burst spectrum does not change during the burst). Thus, the used model was `tbabs*(bbody+diskbb+comptt)`. The values of χ^2 during the first ten seconds tell us that this model does not properly fit the data. This behavior repeats in all the bursts.

To improve the fitting, we tried incorporating a free scaling (f_a) factor to the persistent emission components to account for a possible increase of persistent emission during the burst, as proposed by Worpel et al. (2013, 2015). The f_a factor is implemented as a multiplicative constant in XSPEC that is free to vary during the fitting. Two cases were studied, `constant*(diskbb+comptt)`, and `constant*diskbb+comptt`.

We compare in Fig. 5 the results obtained using the f_a models with those obtained when the persistent emission is considered constant during the bursts. The plot is shown for burst #5, but the same behavior is observed in all the bursts. The figure shows that both f_a models improve the fit with respect to the persistent emission model during the first 10 seconds of the burst. We note, however, that our models do not allow the selection of one f_a model over the other.

3.3.2. Neutron star atmosphere model

We also attempted to use a more detailed description of the NS atmosphere and fit the burst spectra using the NS atmosphere model `burstatmo` proposed by Suleimanov et al. (2011, 2012). This model takes into account Compton scattering in the NS atmosphere, which modifies the burst spectrum to something close to a diluted blackbody. The model used was then `tbabs*(burstatmo+diskbb+comptt)`. Parameters of `diskbb+comptt` were fixed at the pre-burst values. The parameters of the `burstatmo` model are the radius (R), the ratio of the luminosity to the Eddington luminosity ($L/L_{\rm Edd}$), the distance in kpc, the logarithm of surface gravity ($\log g$), the chemical composition, and the normalization. The model is computed on a grid of 18 combinations of chemical composition and gravities: six chemical compositions (pure hydrogen $X = 1$, pure helium $Y = 1$, and four sets of a solar mix of hydrogen and helium with various heavy element abundances) and three gravities $\log g$: 14.0, 14.3, and 14.6. For each combination, 26–28 models are computed for different Eddington ratios (i.e., luminosities in units of the Eddington one). While this grid constrains the flexibility of the model, it is sufficient to cover the typical range of neutron star masses and radii. In Nättilä et al. (2017), this model was used to perform NS mass-radius measurements from the evolution of X-ray burst spectra and the radius of the NS in 4U 1702−429 was estimated to be $R = 12.4 \pm 0.4$ km (68% credibility).

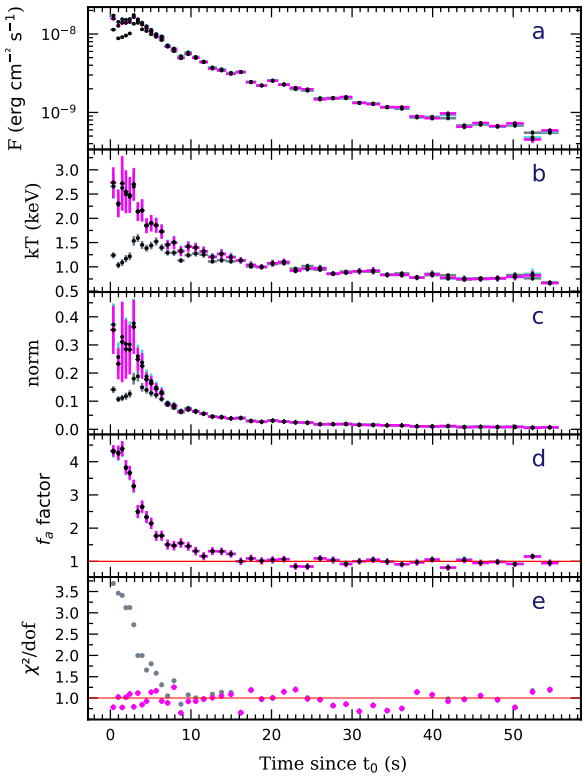

Fig. 5. Time-resolved spectroscopy using the f_a model for burst #4. Results for other bursts are shown in Fig. A.2. Gray markers are used for the blackbody model, and magenta markers are used for the first f_a case, `constant*(diskbb+comptt)`, and cyan markers for the second f_a case, `constant*diskbb+comptt`. Since their behavior is similar, the magenta markers overlap the cyan ones. Panel a shows the estimated bolometric flux, panel b shows the time evolution of the blackbody temperature, panel c shows the time evolution of the blackbody normalization, panel d shows the evolution of the f_a factor, and panel e gives the reduced χ^2 fit statistic. Time is relative to the burst onset (t_0).

For this study, the Eddington ratio and the normalization were the only parameters used for the fitting. Regarding the other parameters, a distance of 10.7 kpc is assumed (Baumgardt & Vasiliev 2021) and the chemical composition was set to pure helium. After testing different combinations of R and $\log g$, we obtained the best-fit results using $R = 14.0$ km and $\log g = 14.6$, which are then used for the fitting. The fitting results are represented in Fig. 6.

The figure shows that the model still does not yield good fits for the first 6 s of the burst if the persistent emission is tied to pre-burst values. We also note that the normalization deviates significantly from unity, especially during the first 6 s, which would indicate strong anisotropy of the burst emission and is

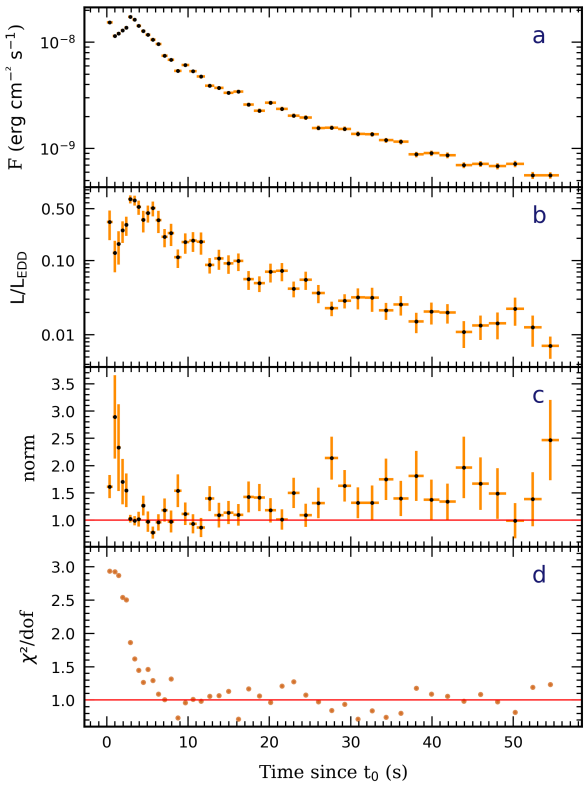

Fig. 6. Time-resolved spectroscopy using the NS atmosphere model for burst #4. Results for other bursts are shown in Fig. A.3. Panel a shows the estimated bolometric flux, panel b shows the time evolution of the ratio of luminosity to the Eddington luminosity, panel c shows the time evolution of the normalization, and panel d gives the reduced χ^2 fit statistic. Time is relative to the burst onset (t_0).

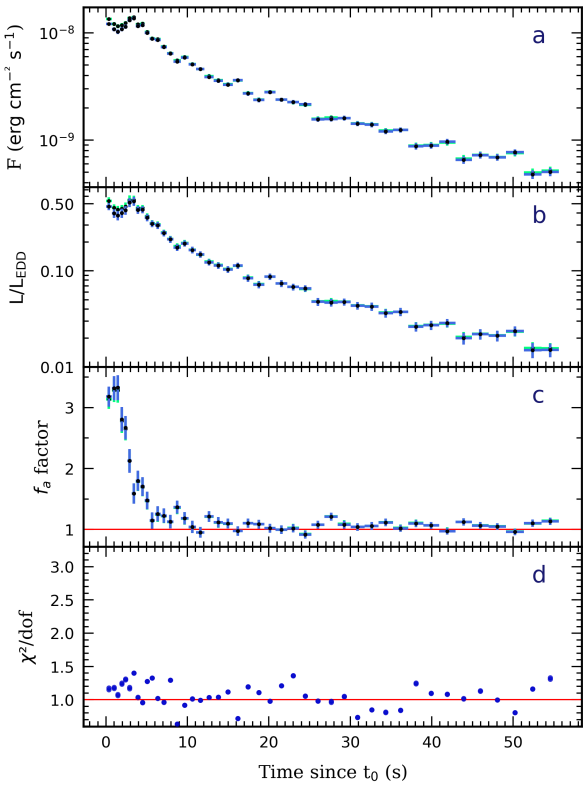

Fig. 7. Time-resolved spectroscopy using the NS atmosphere model in addition to the f_a correction for burst #4. Results for other bursts are shown in Fig. A.4. Blue markers are used for the first f_a case, `constant*(diskbb+comptt)` and light green markers for the second f_a case, `constant*diskbb+comptt`. Since their behavior is similar, the blue markers overlap the green ones. Panel a shows the estimated bolometric flux, panel b shows the time evolution of the ratio of luminosity to Eddington luminosity, panel c shows the evolution of the f_a factor, and panel d gives the reduced χ^2 fit statistic.

likely unphysical. This behavior appears in all the other bursts (see Fig. A.3).

To improve the fitting, we tried incorporating a free scaling (f_a) factor to the pre-burst spectrum when fitting the burst spectra using the NS atmosphere model. Two cases were studied, `constant*(diskbb+comptt)` and `constant*diskbb+comptt`. To do this, we fixed the `burstatmo` normalization to one. The results for burst #4 are shown in Fig. 7. This figure shows both f_a models correct the fit. This behavior appears in all the other bursts (see Fig. A.4).

Figure 8 compares the residuals of the first second of burst #4 for the four different models (see Fig. A.5 for other bursts). This figure corroborates how the f_a models improve the fitting in both scenarios, and also shows the NS atmosphere models give slightly better residuals than the blackbody, but not enough to get a good fit.

4. Discussion

This study analyzes seven M15 X-2 bursts detected by NICER during its 2022 outburst. We observed a significant spectral deviation from the blackbody model in the first few seconds of all the bursts and tested various models to improve the spectral fits. We also constrained the burst recurrence time, which will allow us to estimate the fuel composition. We now discuss these findings.

4.1. Spectral state of the outburst

All the M15 X-2 bursts seem to have occurred in the soft spectral state, as can be inferred from the spectra of their persistent emission (Fig. 2) and outburst hardness evolution (Fig. 1). This contrasts with previous bursts from this source; the 1989 and 2011 outbursts seem consistent with the hard state (van Paradijs et al. 1990; Miller-Jones et al. 2011). The features of these bursts are also notably different from previous ones, with the van Paradijs et al. (1990) and Smale (2001) bursts being particularly powerful and displaying photospheric radius expansion (PRE). Thus, it is plausible that this new set of bursts occurred in a different accretion regime.

4.2. Burst spectral evolution

Time-resolved spectroscopy indicates that all the bursts analysed in this work exhibit enhanced persistent emission during the initial seconds since burst onset. In recent years, NICER's sensitivity to soft X-rays has enabled the detection of many such cases (e.g., Keek et al. 2018a,b; Jaisawal et al. 2019; Bult et al. 2019; Güver et al. 2022a,b; Bult et al. 2022; Yu et al. 2024; Lu et al. 2024). However, this is the first time bursts from this source have been observed with such low-energy coverage.

Figures 5 and A.2 shows that the f_a factor improves the blackbody model fitting of the first ten seconds. The peak val-

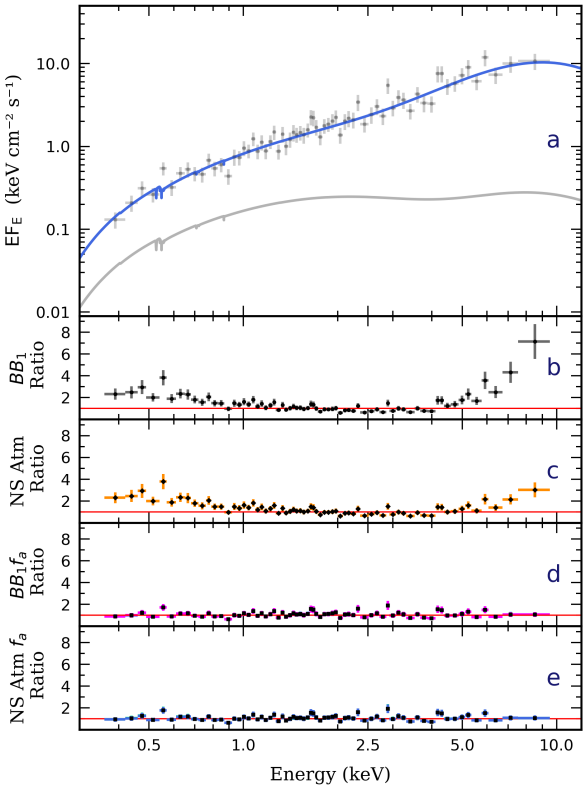

Fig. 8. Burst spectral energy distribution and residuals of the first second of burst #4 when fitted by the four used models. Results for other bursts are shown in Fig. A.5. Panel a shows the spectrum, with the continuous blue line representing the NS atmosphere with f_a factor model, the continuous gray line representing the pre-burst emission model shown in Fig. 2, and the gray points representing the data. Panel b shows the residuals for the blackbody model. Panel c shows the residuals for the NS atmosphere model. Panel d shows the residuals for the blackbody with f_a factor model, with magenta for the `constant*(diskbb+comptt)` case and cyan for `constant*diskbb+comptt` case, both with square markers. Since their behavior is similar, the magenta markers overlap the cyan ones. Panel e shows the residuals of the NS atmosphere with f_a factor model.

ues of f_a that we derive in this work are consistent with those found by Worpel et al. (2015) for non-PRE bursts. After those initial ten seconds, f_a returns to unity, which is consistent with previous studies although the precise duration seems to vary in each case (e.g., Bult et al. 2022).

This enhanced persistent emission, indicated by the f_a correction, is typically interpreted as resulting from an increased accretion rate due to Poynting-Robertson drag (Worpel et al. 2013, 2015). An alternative interpretation proposed by Koljonen et al. (2016) and Kajava et al. (2017) for bursts in the soft state is that there may be a broadening of the spectrum of the spreading layer between the NS surface and the accretion disk. This broadening could resemble an increased accretion rate.

4.3. NS atmosphere models

By fitting the spectra using the NS atmosphere models, we examined whether the blackbody deviations could be explained solely by the bursts' intrinsic spectra. Successful fits with NS atmosphere models can provide accurate mass-radius measurements, as demonstrated by Nättilä et al. (2017). However, Figs. 6 and A.3 show that chi-square values during the first ten seconds of the burst remain poor.

Similar to the blackbody model, the fit improves when the f_a correction is applied, as seen in Figs. 7 and A.4. The residuals in Figs. 8 and A.5 indicate no notable difference between the blackbody and NS atmosphere f_a corrections. We note that in this case, f_a returns to unity in around seven seconds, slightly quicker than with the blackbody model, suggesting that the NS atmosphere model might better represent the intrinsic spectrum. These results indicate that enhanced persistent emission likely masks the intrinsic characteristics of the burst spectrum, making the data unsuitable for precise mass-radius measurements.

We checked if the relative NS luminosity, $L/L_{\rm Edd}$, results for the f_a-corrected NS atmosphere model were similar to the flux values obtained. In this way, we were able to check whether the model was self-consistent. The model's $L/L_{\rm Edd}$ is measured at the NS surface (Suleimanov et al. 2012). The Eddington luminosity of the surface of the NS is defined as:

$$L_{\rm Edd} = \frac{4\pi GMc}{\kappa_{\rm e}}(1+z), \tag{2}$$

where $\kappa_{\rm e}$ is the Thomson scattering opacity. In the case of a He-fueled burst, this becomes:

$$L_{\rm Edd}^{\rm He} = 2L_{\rm Edd}^{\rm H} = 2.52\times10^{38}\frac{M}{M_\odot}(1+z)\ {\rm erg\ s^{-1}}. \tag{3}$$

The gravitational redshift is related to the NS parameters as:

$$1+z = \left(1-2GM/c^2R\right)^{-1/2}. \tag{4}$$

The luminosity at the surface L can then be related to the observed luminosity $L_{\rm obs}$ as follows:

$$L_{\rm obs} = L\,(1+z)^{-2}, \tag{5}$$

and the observed luminosity can be estimated from the observed flux:

$$L_{\rm obs} = 4\pi D^2 F_{\rm obs}, \tag{6}$$

where D is the distance.

Assuming a NS of $M = 1.4M_\odot$, and using the observed flux from the first second of the burst #6 and 10.7 kpc for the distance (Baumgardt & Vasiliev 2021), we obtain $L/L_{\rm Edd} \sim 0.66$. The results, which match well with the values observed in Fig. 7, show the model's estimation makes physical sense. These sub-Eddington luminosities also reflect the lack of observed PRE from any of the bursts.

Finally, it is worth noting that this model assumes the NS does not rotate. However, NSs in LMXBs are typically rapidly rotating (see Galloway & Keek 2021, for a review). Rapid rotation causes the NS shape to be oblate, leading to variations of the local gravity, the emitted flux, the redshift, and the Doppler shift on latitude. All these effects tend to broaden the spectrum (Bauböck et al. 2015; Suleimanov et al. 2020). Therefore, the possibility that the deviations from the blackbody model are due to the effects of a rapidly rotating NS cannot be ruled out and warrants further investigation. Although addressing this is beyond the scope of this work, it offers a basis for future efforts to develop and test models for rotating NS atmospheres.

4.4. X-ray burst fuel

To study the fuel composition, we calculated the ratio of the persistent fluence between bursts to the total burst fluence:

$$\alpha = \frac{F_{\rm per}\Delta T_{\rm rec}}{E_{\rm b}}. \quad (7)$$

We determined that the recurrence timescale, $\Delta T_{\rm rec}$, is the time between the two consecutive bursts shown in Fig. 4, which is ~12.5 h. There are no previous constraints on the recurrence time of M15 X-2 in the literature, except for a lower limit of 1.9 d proposed by White & Angelini (2001).

The persistent flux was then obtained from our spectral analysis of the persistent emission before burst #3 and the total burst fluence was calculated by integrating all the flux values throughout burst #3. To account for the remaining tail of the flux beyond the end of the pointing, we integrated Eq. (1) using its fitted parameters from the end of the exposure to infinity. However, this additional contribution was negligible, falling within the margin of error. We ultimately determined $\alpha = 119 \pm 8$. These values indicate a He-rich burst (Lewin et al. 1993). This is consistent with the rapid burst rise and decay times listed in Table 3, which are characteristic of helium and soft-state bursts (Galloway & Keek 2021). The fuel composition is compatible with UCXB systems, defined by their low hydrogen content. UCXBs have three potential donor channels: the white dwarf (WD) channel, the helium star channel, and the evolved main-sequence star channel (see Nelemans & Jonker 2010, for a review).

Our findings are in agreement with Dieball et al. (2005), who found ultraviolet (FUV) evidence of C and/or He lines, but do not constrain the donor any further. Later studies seem to favor a WD companion: Koliopanos et al. (2021) analyzed the X-ray spectrum of M15 X-2 and noted the absence of Fe Kα emission, suggesting a C/O or O/Ne/Mg WD donor. Armas Padilla et al. (2023) cataloged all known UCXBs, and from the statistical analysis, proposed globular cluster sources usually follow the WD channel and galactic field sources the helium star channel. Typical WDs have an outer layer of residual helium comprising around 1% of the star's total mass (Saumon et al. 2022). In the case of hybrid He-CO WDs, this percentage rises to 2–25% (Zenati et al. 2019). Thus, the presence of helium does not have to be fully discarded in the case of a WD companion, but the exact nature of the donor remains unclear.

The determination of the fuel composition, together with more precise distance measurements, could potentially allow us to reprocess historical bursts from this source with greater accuracy, such as those observed by the *Ginga* satellite (van Paradijs et al. 1990).

5. Conclusions

Using NICER observations, we detected seven X-ray bursts from M15 X-2 during its 2022 outburst. We obtained light curves of the outburst and the individual bursts and performed X-ray spectroscopy of the persistent emission and time-resolved X-ray spectroscopy of the bursts. Below, we discuss the main conclusions of the study.

1. All the bursts have very similar morphology, with quick rises of under a second, decays of tens of seconds, and no evidence of PRE. The spectra of the persistent emission indicate all of the bursts occurred in the soft state.
2. Time-resolved spectroscopy showed all the bursts exhibit enhanced persistent emission in the first few seconds. This behavior was adequately modeled using the $f_{\rm a}$ factor method.
3. NS atmosphere models did not significantly improve the fits in comparison to the blackbody model. This suggests that enhanced persistent emission likely masks the intrinsic characteristics of the burst spectrum, making the data unsuitable for precise mass-radius measurements.
4. Two consecutive bursts allowed us to derive a recurrence time of 12.5 h. Using this recurrence, we estimated the fuel composition by calculating the alpha parameter and obtained $\alpha = 119 \pm 8$, which is consistent with a He-rich burst. This result is in accordance with the UCXB nature of the source.

Acknowledgements. We thank the anonymous referee for their feedback that helped improve the manuscript. MADT acknowledges support from the EDUFI Fellowship and the Johannes Andersen Student Programme at the Nordic Optical Telescope. We acknowledge support from ESA through the ESA Space Science Faculty Visitor scheme (ESA-SCI-SC-LE-098 and ESA-SCI-SC-LE-203). M.N. is a Fonds de Recherche du Quebec – Nature et Technologies (FRQNT) postdoctoral fellow.

References

Armas Padilla, M., Corral-Santana, J. M., Borghese, A., et al. 2023, A&A, 677, A186
Arnaud, K. A. 1996, in Astronomical Data Analysis Software and Systems V, eds. G. H. Jacoby, & J. Barnes (San Francisco: ASP), ASP Conf. Ser., 101, 17
Ballantyne, D. R., & Everett, J. E. 2005, ApJ, 626, 364
Bauböck, M., Özel, F., Psaltis, D., & Morsink, S. M. 2015, ApJ, 799, 22
Baumgardt, H., & Vasiliev, E. 2021, MNRAS, 505, 5957
Bult, P., Jaisawal, G. K., Güver, T., et al. 2019, ApJ, 885, L1
Bult, P., Mancuso, G. C., Strohmayer, T. E., et al. 2022, ApJ, 940, 81
Charles, P. A., Clarkson, W. I., & van Zyl, L. 2002, New A, 7, 21
Cumming, A., Macbeth, J., in't Zand, J. J. M., & Page, D. 2006, ApJ, 646, 429
Degenaar, N., Miller, J. M., Wijnands, R., Altamirano, D., & Fabian, A. C. 2013, ApJ, 767, L37
Dieball, A., Knigge, C., Zurek, D. R., et al. 2005, ApJ, 634, L105
Done, C., Gierliński, M., & Kubota, A. 2007, A&A Rev., 15, 1
Fujimoto, M. Y., Hanawa, T., & Miyaji, S. 1981, ApJ, 247, 267
Galloway, D. K., & Keek, L. 2021, in Timing Neutron Stars: Pulsations, Oscillations and Explosions, eds. T. M. Belloni, M. Méndez, & C. Zhang (Berlin, Heidelberg: Springer), ASSL, 461, 209
Grindlay, J., Gursky, H., Schnopper, H., et al. 1976, ApJ, 205, L127
Güver, T., Bostancı, Z. F., Boztepe, T., et al. 2022a, ApJ, 935, 154
Güver, T., Boztepe, T., Ballantyne, D. R., et al. 2022b, MNRAS, 510, 1577
Heger, A., Cumming, A., Galloway, D. K., & Woosley, S. E. 2007, ApJ, 671, L141
Heinke, C. O., Cohn, H. N., & Lugger, P. M. 2009, ApJ, 692, 584
Heinke, C. O., Zheng, J., Maccarone, T. J., et al. 2024, arXiv e-prints [arXiv:2407.18867]
Homan, J., van den Berg, M., Heinke, C., & Pooley, D. 2022, ATel, 15640, 1
in't Zand, J. J. M., Galloway, D. K., & Ballantyne, D. R. 2011, A&A, 525, A111
in't Zand, J. J. M., Galloway, D. K., Marshall, H. L., et al. 2013, A&A, 553, A83
in't Zand, J. J. M., Visser, M. E. B., Galloway, D. K., et al. 2017, A&A, 606, A130
Jaisawal, G. K., Chenevez, J., Bult, P., et al. 2019, ApJ, 883, 61
Kajava, J. J. E., Koljonen, K. I. I., Nättilä, J., Suleimanov, V., & Poutanen, J. 2017, MNRAS, 472, 78
Keek, L., Arzoumanian, Z., Bult, P., et al. 2018a, ApJ, 855, L4
Keek, L., Arzoumanian, Z., Chakrabarty, D., et al. 2018b, ApJ, 856, L37
Koliopanos, F., Péault, M., Vasilopoulos, G., & Webb, N. 2021, MNRAS, 501, 548
Koljonen, K. I. I., Kajava, J. J. E., & Kuulkers, E. 2016, ApJ, 829, 91
Kuulkers, E., den Hartog, P. R., in't Zand, J. J. M., et al. 2003, A&A, 399, 663
Lewin, W. H. G., van Paradijs, J., & Taam, R. E. 1993, Space Sci. Rev., 62, 223
London, R. A., Taam, R. E., & Howard, W. M. 1986, ApJ, 306, 170
Lu, Y., Li, Z., Yu, W., Pan, Y., & Falanga, M. 2024, ApJ, 969, 15
Makishima, K., Maejima, Y., Mitsuda, K., et al. 1986, ApJ, 308, 635
Miller-Jones, J. C. A., Sivakoff, G. R., Heinke, C. O., et al. 2011, ATel, 3378, 1
Nättilä, J., Miller, M. C., Steiner, A. W., et al. 2017, A&A, 608, A31
Nelemans, G., & Jonker, P. G. 2010, New Astron. Rev., 54, 87
Nelemans, G., Jonker, P. G., & Steeghs, D. 2006, MNRAS, 370, 255
Nelson, L. A., Rappaport, S. A., & Joss, P. C. 1986, ApJ, 304, 231
Ng, M., Sanna, A., Bult, P. M., et al. 2022, ATel, 15593, 1
Pike, S. N., Harrison, F. A., Tomsick, J. A., et al. 2021, ApJ, 918, 9

Pooley, D., & Homan, J. 2013, ATel, 5490, 1
Remillard, R. A., Loewenstein, M., Steiner, J. F., et al. 2022, AJ, 163, 130
Revnivtsev, M. G., & Gilfanov, M. R. 2006, A&A, 453, 253
Sánchez-Fernández, C., Kajava, J. J. E., Poutanen, J., Kuulkers, E., & Suleimanov, V. F. 2020, A&A, 634, A58
Saumon, D., Blouin, S., & Tremblay, P.-E. 2022, Phys. Rep., 988, 1
Sidoli, L., Parmar, A. N., & Oosterbroek, T. 2000, A&A, 360, 520
Sivakoff, G. R., Heinke, C. O., Miller-Jones, J. C. A., et al. 2011, ATel, 3393, 1
Smale, A. P. 2001, ApJ, 562, 957
Strohmayer, T., & Bildsten, L. 2006, in Compact stellar X-ray sources, eds. W. Lewin, & M. van der Klis (Cambridge: Cambridge University Press), Cambridge Astrophys. Ser., 39, 113
Strohmayer, T. E., & Brown, E. F. 2002, ApJ, 566, 1045
Suleimanov, V., Poutanen, J., Revnivtsev, M., & Werner, K. 2011, ApJ, 742, 122
Suleimanov, V., Poutanen, J., & Werner, K. 2012, A&A, 545, A120
Suleimanov, V. F., Poutanen, J., & Werner, K. 2020, A&A, 639, A33
Titarchuk, L. 1994, ApJ, 434, 570
Tomida, H., Ueno, S., Serino, H. N. M., et al. 2013, ATel, 5327, 1
van Paradijs, J., Dotani, T., Tanaka, Y., & Tsuru, T. 1990, PASJ, 42, 633
White, N. E., & Angelini, L. 2001, ApJ, 561, L101
Wilms, J., Allen, A., & McCray, R. 2000, ApJ, 542, 914
Worpel, H., Galloway, D. K., & Price, D. J. 2013, ApJ, 772, 94
Worpel, H., Galloway, D. K., & Price, D. J. 2015, ApJ, 801, 60
Yu, W., Li, Z., Lu, Y., et al. 2024, A&A, 683, A93
Yungelson, L. R., Nelemans, G., & van den Heuvel, E. P. J. 2002, A&A, 388, 546
Zenati, Y., Toonen, S., & Perets, H. B. 2019, MNRAS, 482, 1135

Appendix A: Additional figures

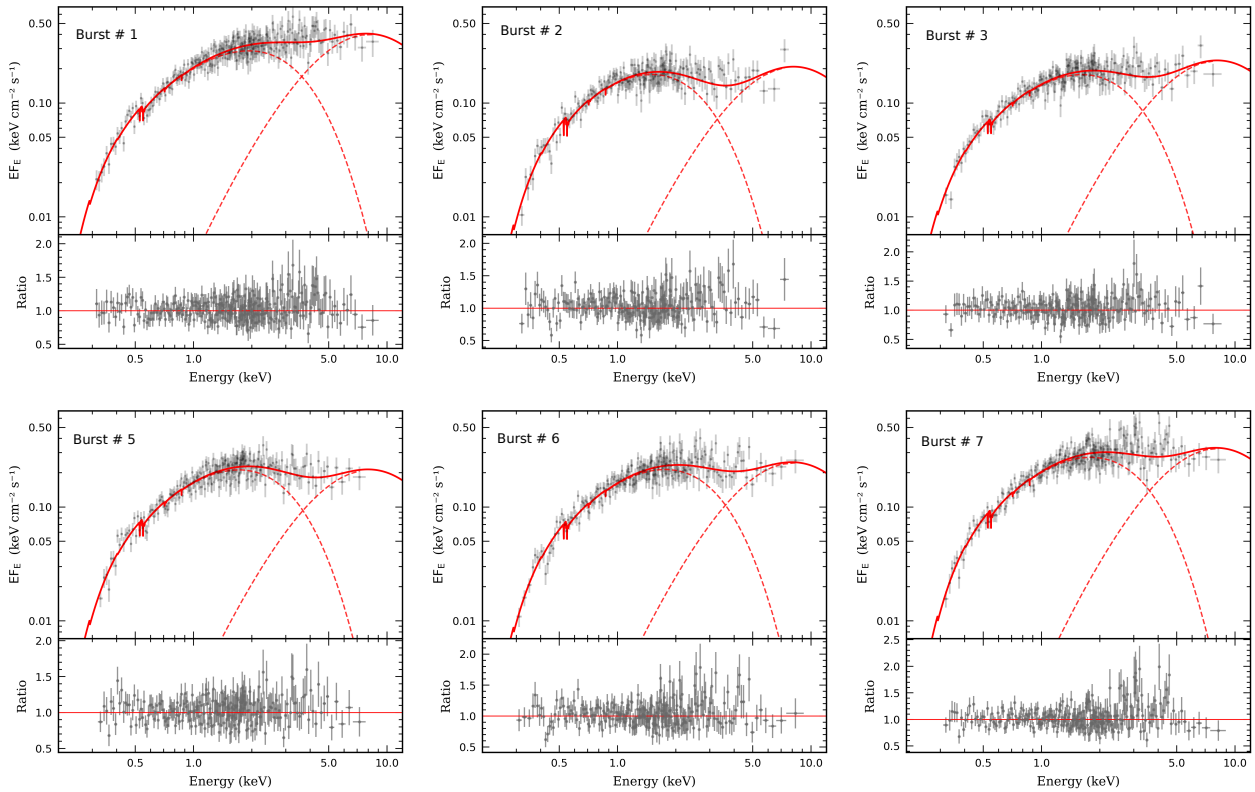

Fig. A.1. Same as Fig. 2 but for different bursts labeled on the figure.

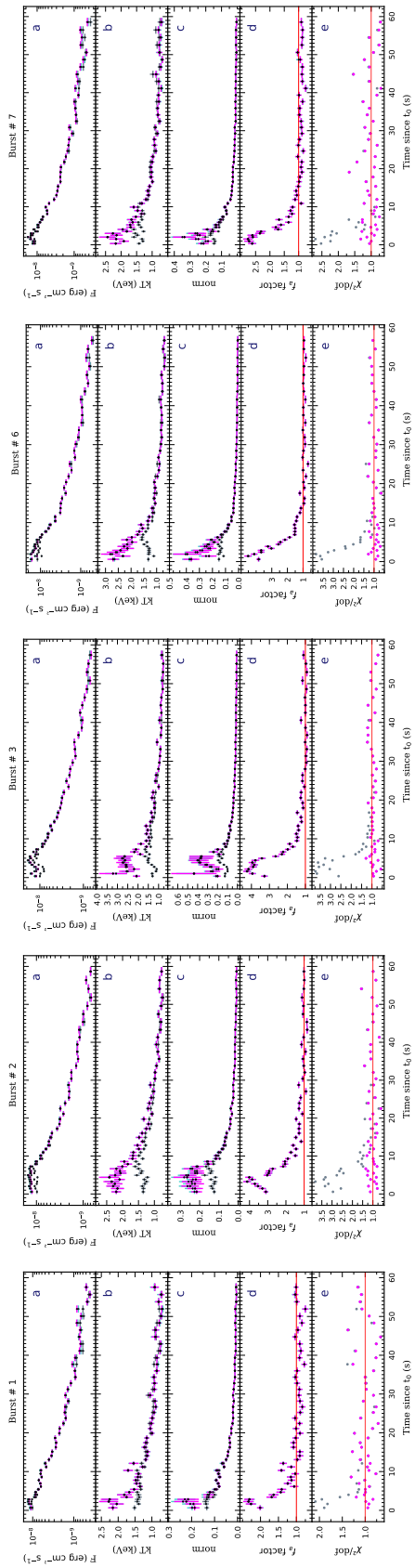

Fig. A.2. Same as Fig. 6 but for different bursts labeled on the figure.

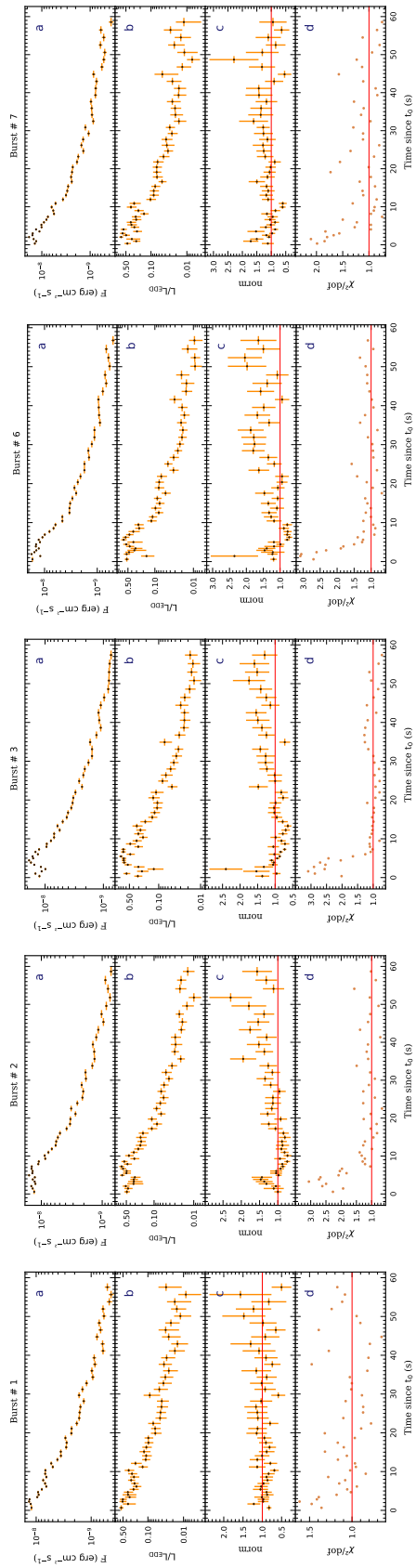

Fig. A.3. Same as Fig. 6 but for different bursts labeled on the figure.

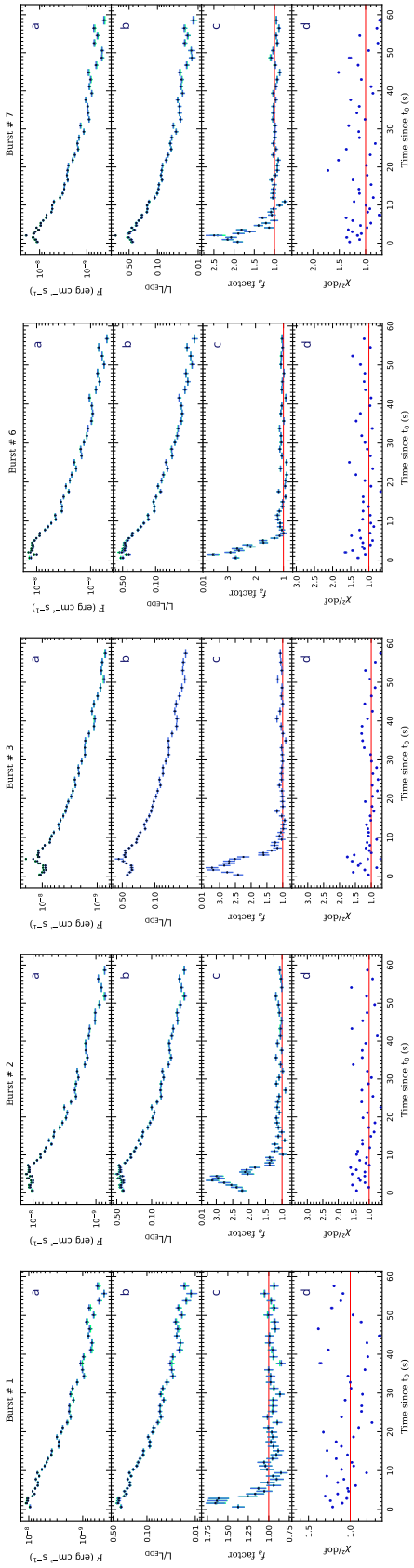

Fig. A.4. Same as Fig. 7 but for different bursts labeled on the figure.

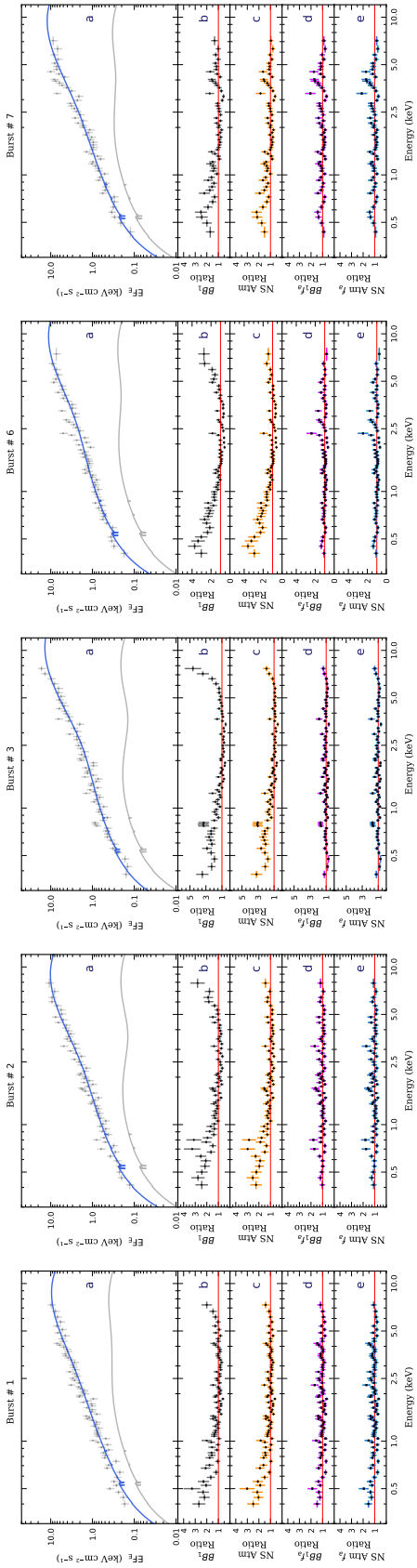

Fig. A.5. Same as Fig. 8 but for different bursts labeled on the figure.